

The artificial night sky brightness mapped from DMSP satellite Operational Linescan System measurements

P. Cinzano,¹★ F. Falchi,¹ C. D. Elvidge² and K. E. Baugh²

¹*Dipartimento di Astronomia, Università di Padova, vicolo dell'Osservatorio 5, I-35122 Padova, Italy*

²*Solar-Terrestrial Physics Division, NOAA National Geophysical Data Center, 3100 Marine Street, Boulder, CO 80303, USA*

Accepted 2000 March 17. Received 1999 December 7

ABSTRACT

We present a method to map the artificial sky brightness across large territories in astronomical photometric bands with a resolution of approximately 1 km. This is of use in quantifying the situation regarding night sky pollution, recognizing potential astronomical sites and allowing future monitoring of trends. The artificial sky brightness present in the chosen direction at a given position on the surface of the Earth is obtained by the integration of the contributions produced by every surface area in the surroundings. Each contribution is computed via detailed models for the propagation in the atmosphere of the upward light flux emitted by the area. The light flux is measured with top-of-atmosphere radiometric observations made by the Defense Meteorological Satellite Program (DMSP) Operational Linescan System.

We have applied the described method to Europe, obtaining maps of artificial sky brightness in the *V* and *B* bands.

Key words: scattering – atmospheric effects – light pollution – site testing.

1 INTRODUCTION

The night sky is a world heritage. In recent decades there has been a rapid increase in the brightness of the night sky in nearly all countries. This has degraded astronomical viewing conditions. The increase in night sky brightness is one of the most noticeable effects of light pollution, which can be defined as the alteration of natural light levels in the outdoor environment owing to artificial light sources. The widespread use of artificial lighting with little regard to fixture shielding or energy conservation is the primary source of light owing to mankind's responsibility contributing to the brightness of the night sky. The astronomical community has expressed its concern over the growth of the sky brightness in a number of official documents and positions [e.g. the Resolutions of the General Assemblies of the International Astronomical Union (IAU) XVI/9 1976, XIX/B6 1985, XX/A2 1988 and XXIII/A1 1997, and the Positions of the American Astronomical Society]. UNESCO, the United Nations and the Commission Internationale de l'Éclairage (CIE) give consideration to these concerns. Commission 50 of the IAU (The Protection of Existing and Potential Astronomical Sites) is working actively in order to preserve the astronomical sky, and many studies and meetings have been dedicated to this topic (e.g. Crawford 1991; Kovalevsky 1992; McNally 1994; Isobe & Hirayama 1998; Cinzano 2000a; see also Cinzano 1994 for a large reference list). Laws, bills, standard rules, ordinances and regulations limit in many countries the direct wasting

of light in the sky from lighting fixtures and, in some cases, also the quantity of light reflected by lighted surfaces. The International Dark-Sky Association is active worldwide in this battle of culture and intelligence, with the aim of building awareness and saving for mankind the possibility of feeling part of the Universe.

An effective battle against light pollution requires knowledge of the condition of the night sky across large territories, recognition of vulnerable areas, determination of growth trends, and identification of the most polluting cities. Therefore a method of mapping the artificial sky brightness across large territories is required. This is also of use in recognizing areas with low levels of light pollution and potential astronomical sites. In the past, mappings of sky brightness for extended areas have been performed using population density data with some simple modelling. Examples include the works of Walker (1970, 1973) in California and Arizona, Albers (1998) in the USA, Bertiau, de Graeve & Treanor (1973) in Italy, and Berry (1976) and Pike (1976) in Ontario (Canada). These authors used population data of cities to estimate their upward light emission, and a variety of empirical or semi-empirical propagation laws for light pollution in order to compute the sky brightness produced by them. Recently, advances in the availability and gain control of the Defense Meteorological Satellite Program (DMSP) satellite have provided direct measurements of the upward light emission from nearly the entire surface of the Earth (60° south to 72° north). The first global DMSP image of the Earth at night was produced at 10-km resolution (Sullivan 1989, 1991) using DMSP film strips, the only data available at that time. Beginning in 1992, the availability

★ E-mail: cinzano@pd.astro.it

of digital DMSP data has enabled a new set of higher spatial resolution products (Elvidge et al. 1997a,b,c). These data have been used to model population distribution (Sutton et al. 1997) and the impact of urban sprawl on food production (Imhoff et al. 1997a,b). The data have also been used to document light pollution as expressed in the increase in the upward flux of light over time for Japan (Isobe & Hamamura 1998).

In this paper we present a method of mapping the artificial sky brightness across large territories. In order to bypass errors arising when using population data to estimate upward flux, we construct the maps by direct measurements of the upward flux as observed from space using DMSP satellite night-time images, and compute the downward flux to the surface of the Earth with detailed modelling of light pollution propagation in the atmosphere. We also present, as an application, detailed maps of artificial sky brightness in Europe in the *V* and *B* astronomical photometric bands with a resolution of approximately 1 km. In Section 2 we describe the OLS-DMSP satellite observations, their reduction and analysis. We also discuss the relation of upward flux versus city population. In Section 3 we describe the mapping technique and in Section 4 we discuss its application to the maps of Europe. The maps are presented in Section 5, together with our comments. Section 6 contains our conclusions.

2 OBSERVATIONS AND DATA ANALYSIS

2.1 Satellite data

US Air Force DMSP satellites are in low-altitude (830 km) Sun-synchronous polar orbits with an orbital period of 101 min. With 14 orbits per day they generate a global night-time and day-time coverage of the Earth every 24 h with their main purpose to monitor the distribution of clouds and to assess navigation conditions. The US Department of Commerce, National Oceanic and Atmospheric Administration (NOAA) National Geophysical Data Center (NGDC) serves as the archive for the DMSP. The digital archive was initiated in 1992. Starting in 1994, NGDC has embarked on the development of night-time light processing algorithms and products from the DMSP-OLS (Elvidge et al. 1997a,b,c).

The Operational Linescan System (OLS) is an oscillating scan radiometer with low-light visible and thermal infrared (TIR) imaging capabilities, which first flew on DMSP satellites in 1976. At night the OLS uses a photomultiplier tube (PMT) to intensify the visible band signal. The purpose of this intensification is to observe clouds illuminated by moonlight. The PMT data have a broad spectral response from 440 to 940 nm (485–765 nm FWHM) with highest sensitivity in the 500–650 nm region (see Fig. 1). This covers the range for primary emissions from the most widely used lamps for external lighting: mercury vapour (545 and 575 nm), high-pressure sodium (from 540 to 630 nm), and low-pressure sodium (589 nm). The sensitivity of the PMT, combined with the OLS-VDGA (variable digital gain amplifier) and fixed-gain OLS pre- and post-amplifiers, allows measurement of radiances down to $10^{-10} \text{ W cm}^{-2} \text{ sr}^{-1} \mu\text{m}^{-1}$ (Elvidge et al. 1999). This implies that the OLS-PMT could detect radiation with an effective wavelength near 550 nm down to a luminance of approximately 0.2 mcd m^{-2} . The TIR detector is sensitive to radiation from 10.0 to 13.4 μm (10.3–12.9 μm FWHM).

The OLS acquires swaths of data that are 3000 km wide. The OLS sinusoidal scan maintains a nearly constant along-track pixel-to-pixel ground sample distance (GSD) of 0.56 km. Likewise, the electronic sampling of the signal from the individual

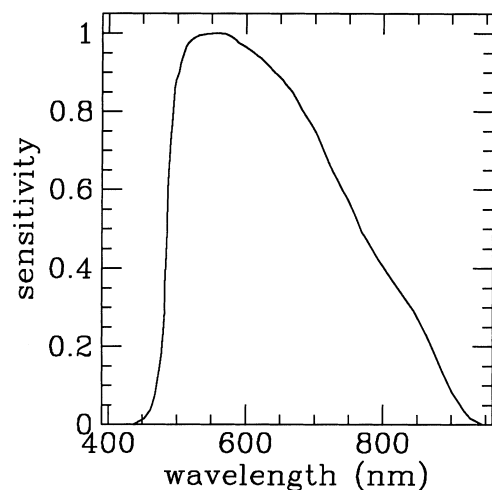


Figure 1. Spectral sensitivity of the OLS-PMT detector of DMSP satellite F12.

scan lines maintains a GSD of 0.56 km. The effective instantaneous field of view (EIFOV) is larger than the 0.56-km GSD, and varies with scan angle. At nadir the EIFOV is 2.2 km and expands to 5.4 km at the edge of scan 1500 km out from nadir. Most of the data received by NGDC have been ‘smoothed’ by on-board averaging of 5×5 pixel blocks, yielding data with a GSD of 2.8 km. Other details of the OLS are described by Lieske (1981).

DMSP platforms are stabilized using four gyroscopes (three-axis stabilization), and platform orientation is adjusted using a star mapper, an Earth limb sensor, and a solar detector (Elvidge et al. 1997a). Daily radar bevel vector sightings of the satellites provided by Naval Space Command allow Air Force orbital mechanics models to compute the geodetic subtrack of each orbit, giving the positions of satellites every 0.4208 s. These positions, together with OLS scan angle equations, an oblate ellipsoid Earth sea-level model and digital terrain elevations from the US Geological Survey (USGS) EROS Data Center, allow geolocation algorithms to estimate latitude and longitude for each pixel centre.

Normally the OLS is operated at high gain settings for cloud detection. City lights are saturated in these data and radiances cannot be extracted. In 1996 and 1997, NGDC made special requests to the Air Force for collection of OLS-PMT data at reduced gain settings. This request was granted for the darkest nights of lunar cycles in 1996 March (eight nights) and 1997 January and February (10 nights each). During these experimental data collections, on-board algorithms that adjust the visible band gain were disabled. The major on-board algorithm that affects the night-time visible band data is the along-scan gain control (ASGC), which adjust the gain dynamically in response to scene brightness. There is also a on-board bi-directional reflectance (BRDF) algorithm designed to reduce the brightness of the image ‘hotspot’ which occurs where the observation angle matches the illumination angle. The BRDF algorithm has minimal effect when lunar illumination is low, as was the case during the 28 nights when the gain-controlled data were acquired. The two on-board gain control algorithms were turned off to simplify the retrieval of radiances from the special data collections.

During the special data acquisition the OLS-VDGA gain, which is normally operated at 60 dB, was reduced to avoid saturation in urban centres. On one set of nights the gain was operated at a setting of 24 dB. This produced data that avoided saturation on

major urban centres, but did not permit detection of city edges and lighting in smaller towns. To overcome this dynamic range limitation, data were also acquired at gain settings of 40 and 50 dB.

2.2 Data reduction

These data were used to assemble a cloud-free composite image calibrated to top-of-atmosphere (TOA) radiances. The composition provides additional advantages in the removal of ephemeral light sources, such as fire and lightning, plus the retrieval of lights from small towns that are near the detection limits of the sensor and processing algorithms. The primary processing steps include: (i) establishment of a reference grid with finer spatial resolution than the input imagery using the 1-km equal-area Interrupted Homolosine Projection (Goode 1925; Steinwand 1993) developed for the NASA-USGS Global 1-km Advanced Very High Resolution Radiometer (AVHRR) project; (ii) identification of the cloud-free section of each orbit based on OLS-TIR data; (iii) identification of lights, removal of noise and solar glare, cleaning of defective scan lines and cosmic rays; (iv) projection of the lights from cloud-free areas from each orbit into the reference grid; (v) calibration to radiance units using prior-to-launch calibration of digital number for given input telescope illuminance and VDGA gain settings in simulated space conditions; (vi) tallying of the total number of light detections in each grid cell and calculation of the average radiance value and (vii) filtering of images based on frequency of detection to remove ephemeral events.

The final image was transformed into latitude/longitude projection with $30 \times 30 \text{ arcsec}^2$ pixel size with data in eight-bit byte format and power-law scaling (see Elvidge et al. 1999 for details). The maps of Europe described below were obtained from an image extracted from the global image. The image of Europe is 4800×4800 pixels in size, starting at longitude $10^\circ 30'$ west and latitude 72° north. The orbits involved are listed in Appendix B.

The radiance range of the final composite image goes from a minimum of 1.54×10^{-9} to a maximum of $3.17 \times 10^{-7} \text{ W cm}^{-2} \text{ sr}^{-1} \mu\text{m}^{-1}$. The minimum luminance detectable for light with an effective wavelength of 550 nm (the power of which is $1.47 \times 10^{-3} \text{ W lm}^{-1}$) is approximately 3 mcd m^{-2} . Assuming an average vertical extinction of $\sim 0.3 \text{ mag}$ in the visual band, the minimum detectable luminance on the ground would be of the order of 4 kcd km^{-2} . Two unshielded fixtures of the ‘globe’ kind, with clean transparent glass (fixture efficiency ~ 80 per cent), equipped with a 250-W high-pressure sodium lamp with 125 lm W^{-1} efficiency, and placed every square kilometre, could be sufficient to produce this luminance.

2.3 Data analysis

We first analysed the composite image in order to evaluate the emission versus population relationship. We chose a number of European cities of various populations¹ and measured their relative upward flux per unit solid angle, summing the counts of all pixels pertinent to each city and multiplying for pixel size at that latitude. Fig. 2 shows the measured upward flux of a sample of European cities normalized, for display purposes, to the average flux of a city of $\sim 10^5$ inhabitants in the same country. The upward emission increases linearly with the population. One possible

¹ Population data refer to 1991 for Italy, Spain and Greece, 1990 for France and 1996 for Germany, and have been provided by their national bureaux of statistics.

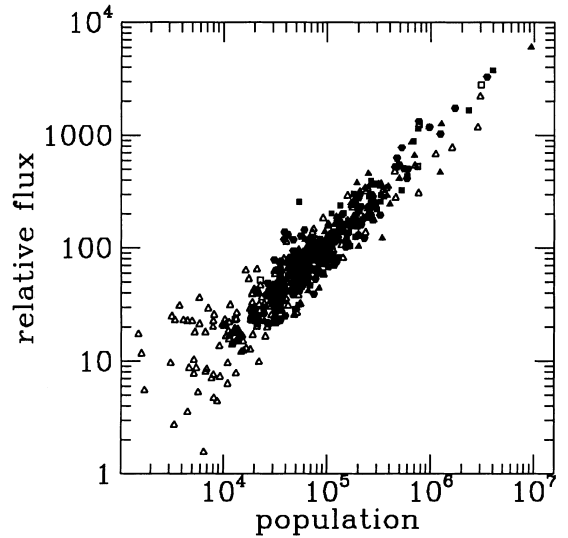


Figure 2. Relationship of normalized upward flux versus city population for Italy (open triangles), France (filled triangles), Germany (filled circles), Spain (filled squares) and Greece (open squares).

source of error is the on-board averaging of the 5×5 pixel blocks during the smoothing process. During smoothing it is possible for saturated pixels in the cores of urban centres to be averaged in with unsaturated pixels to produce an unsaturated smoothed pixel value. This phenomenon will be addressed through the inclusion of OLS data acquired at even lower gain settings in the updated night-time lights map that NGDC is preparing for the 1999–2000 time period. Another uncertainty in the city analysis is that we did not precisely match the outline of the lights to the population data reporting area.

Even if the upward emission versus city population relationship depends on the local lighting habits, our results are in agreement with relations successfully applied or measured in other countries. Elvidge et al. (1999) found a linear relation between composite radiance and population for a sample of cities in North America, and obtained a smaller scatter when correlating radiance with electricity consumption. Walker (1977) found linear proportionality between population and street light emission for a number of Californian cities, with a few departures above or below the mean depending on the industrial or residential character of the city. He also measured the sky illumination produced by three cities, obtaining a dependence, to the power of 0.8, on their population. Bertiau et al. (1973) successfully used a linear model with brightness proportional to population to predict light pollution, and so did Walker (1970, 1973) and Garstang (1987, 1988, 1989a,b,c, 1991a,b,c, 1992, 1993, 2000), who obtained a good fit with many observations including Walker’s (1977) population–distance data. Berry (1976) obtained good fits of observations of sky brightness in city centres in Ontario, with a propagation law for light pollution based on the approach of Treanor (1973) but assuming a dependence on the population to the power of 0.5. However, Garstang’s linear models fit Berry’s (1976) observations well, suggesting that the power of 0.5 found by him was produced by the extinction of light emitted by the outskirts of large cities in propagating to the centre, and does not depend on the upward flux versus population relationship (Garstang 1989a).

Bertiau et al. (1973) in the early 1970s found that the upward emission of cities in Italy depended on their economic and commercial development, so they were forced to include in their

model a development factor. 25 years later we are unable to identify an affluence effect on the brightness of Italian cities. Cities in southern Italy have the same light output as cities of comparable size cities in northern Italy, even if the former have a per capita income that is nearly half that of the latter.

The proportionality between satellite data and population would allow us to replace the population distribution from census data, usually adopted in computations of night-sky brightness, with satellite data, independently of the fact that we would be observing light coming from external night-time lighting or whatever other source. This replacement constitutes an improvement, because census data are based on city lists which, although they can be associated with the geographical position of the city, do not provide spatially explicit detail of the geographical distribution of the population.

3 MAPPING TECHNIQUE

Scattering from atmospheric particles and molecules spreads the light emitted upward by the sources. If $e(x, y)$ is the upward emission per unit area in (x, y) , the total artificial sky brightness in a given direction of the sky in a site in (x', y') is

$$b(x', y') = \iint e(x, y) f[(x, y), (x', y')] dx dy, \quad (1)$$

where $f[(x, y), (x', y')]$ gives the artificial sky brightness per unit of upward light emission produced by the unitary area in (x, y) in the site in (x', y') . The light pollution propagation function f depends in general on the geometrical disposition (the altitude of the site and the area, and their mutual distance), on the atmospheric distribution of molecules and aerosols and their optical characteristics in the chosen photometric band, on the shape of the emission function of the source, and on the direction of the sky observed. In some works this function has been approximated with a variety of semi-empirical propagation laws like the Treanor law (Treanor 1973; Falchi & Cinzano 2000; Cinzano et al. 2000), the Walker law (Walker 1973; Joseph, Kaufman & Mekler 1991), the Berry law (Berry 1976; Pike 1976) and the Garstang law (Garstang 1991b).

We have obtained the propagation function $f[(x, y), (x', y')]$ for each couple of points (x, y) and (x', y') with detailed models for the light propagation in the atmosphere based on the modelling technique introduced and developed by Garstang (1986, 1987, 1988, 1989a,b,c, 1991a,b,c, 1992, 1993, 2000) and also applied by Cinzano (2000b,c,d). The models assume Rayleigh scattering by molecules and Mie scattering by aerosols, and take into account extinction along light paths and Earth curvature. These models allow association of the predictions with well-defined parameters related to the aerosol content, so the atmospheric conditions to which predictions refer can be well known. Here we will describe only the main outlines of the models and our specific implementation, leaving the reader to refer to the cited papers for details.

A telescope of area $\pi d^2/4$ situated at observing site O collects, from within an infinitesimal section $dV = (\pi \epsilon^2 u^2 du)$ of the cone of angle 2ϵ around the line of sight at a distance u and with thickness du , a luminous flux $d\Phi$ given by

$$d\Phi = \frac{\pi d^2}{4} \frac{1}{u^2} M_s(u) \xi_1(u) (\pi \epsilon^2 u^2 du), \quad (2)$$

where $M_s(u)$ is the luminous flux scattered in unit solid angle toward the observer from particles of aerosols and molecules

inside unit volume of atmosphere at the distance u along the line of sight, and $\xi_1(u)$ is the extinction of the light along its path to the telescope.

Calling e_s the upward flux of the source and $S = M_s/e_s$ the scattered flux per unit solid angle per unit upward flux, the propagation function f , expressed as total flux per unit area of the telescope per unit solid angle per unit total upward light emission, is found by integrating equation (2) from the site to infinity:

$$f = \int_{u_0}^{\infty} S(u) \xi_1(u) du, \quad (3)$$

with

$$\xi_1 = \exp \left\{ - \int_0^u [N_m(h) \sigma_m + N_a(h) \sigma_a] dx \right\}, \quad (4)$$

where $N_m(h)$ and $N_a(h)$ are respectively the vertical number densities of molecules and aerosols; σ_m and σ_a are their scattering cross-sections. The altitude h depends on the integration variable x , on the zenith distance and azimuth of the line of sight, on the altitudes of site and source, and on their distance.

The luminous flux per unit solid angle per unit upward flux coming *directly* from the source and scattered toward the observer from unit volume along the line of sight is

$$S_d(u) = [N_m(h) \sigma_m f_m(\omega) + N_a(h) \sigma_a f_a(\omega)] i(\psi, s), \quad (5)$$

where $i(\psi, s)$ is the direct illuminance per unit flux produced by each source on each infinitesimal volume of atmosphere along the line of sight of an observer, and $f_m(\omega)$ and $f_a(\omega)$ are the normalized angular scattering functions of molecular and aerosol scattering respectively. The scattering angle ω , the emission angle ψ , the distance s of the section from the source and the altitude h of it depend on the altitudes of the site and the source, their distance, the zenith distance and the azimuth of the line of sight and the distance u along the line of sight, through some geometry.

If $I(\psi)$ is the normalized light flux per unit solid angle emitted by the considered source at zenith distance ψ , and s is the distance between the source and the considered infinitesimal volume of atmosphere, the illuminance per unit flux is

$$i(\psi, s) = I(\psi) \xi_2/s^2 \quad (6)$$

in the range where there is no shielding by Earth curvature, and zero elsewhere. The extinction ξ_2 along the path is

$$\xi_2 = \exp \left\{ - \int_0^s [N_m(h) \sigma_m + N_a(h) \sigma_a] dx \right\}. \quad (7)$$

A single-scattering model is not sufficient to describe the artificial sky brightness produced by a source. In a real atmosphere, several scatterings may occur as a photon travels from the source to the telescope. The optical thickness $\tau = \int k dr$, where k is an attenuation coefficient, determines how important secondary and higher-order scattering is. If $\tau \gg 1$ (thick layer), multiple scattering is dominant. The fraction of incident radiation that has been scattered once is $(1 - e^{-\tau})$, and the fraction that is scattered again is of order $(1 - e^{-\tau})^2$. If $(1 - e^{-\tau})$ is sufficiently small, which happens when τ is small, secondary and higher-order scattering can be neglected. In absence of aerosols the optical thickness of the atmosphere at a wavelength of 550 nm is about 0.1 (Twomey 1977). The aerosol optical thickness can be 0.05 in cleaner regions of the globe, but it can grow to higher values, even depending on seasonal changes (Garstang 1988). Then single scattering is the major contributor to scattered radiation, but

secondary scattering is not negligible. The error in neglecting third- and higher-order scattering can be significant for optical thicknesses higher than about 0.5. Therefore, in the computation of the total light flux S that molecules and aerosols in the infinitesimal volume scatter toward the observer, we take into account light that has already been scattered once. We have assumed, as did Garstang (1984, 1986), that the light coming to the considered infinitesimal volume along the line of sight after a scatter has approximately a direction near that of the direct light, so that the scattering angle ω in the first approximation is always the same. In this case the total illuminance S can be written

$$S = S_d D_S, \quad (8)$$

where D_S is a correction factor which takes into account the illuminance produced by light already scattered once from molecules and aerosols, which can be evaluated with the approach of Treanor (1973) as extended by Garstang (1984, 1986). Details on assumptions can be found in the quoted papers.

4 APPLICATION

In practice, we have divided the surface of Europe into land areas with the same positions and dimensions as projections on the Earth of the pixels of the satellite image. We have assumed each land area to be a source of light pollution with an upward emission $e_{x,y}$ proportional to the radiance measured in the corresponding pixel multiplied by the surface area. The total artificial sky brightness at the centre of each area, given by the expression (1), becomes

$$b_{i,j} = \sum_h \sum_k e_{h,k} f[(x_i, y_j), (x_h, y_k)]. \quad (9)$$

We have obtained the propagation function $f[(x_i, y_j), (x_h, y_k)]$ for each couple of points (x_i, y_j) and (x_h, y_k) , the positions of the observing site and the polluting area, from equation (3) after inserting equations (5) and (6) multiplied by the double scattering factor D_S computed as below in equation (20). We have considered every land area as a point source located at its centre except when $i = h, j = k$, in which case we have used a four-point approximation (Abramowitz & Stegun 1964). The resolution of the maps, depending on results from an integration over a large zone, is greater than the resolution of the original images and is generally of the order of the distance between two pixel centres. However, where sky brightness is dominated by contributions of the nearest land areas, effects of the resolution of the original image could become relevant.

We have obtained maps for the B and V photometric astronomical bands (Johnson 1955).

4.1 Atmospheric model

4.1.1 Molecular atmosphere vertical distribution

We have assumed that the atmosphere is in hydrostatic equilibrium under the gravitational force. Neglecting the curvature of the Earth, the force per unit surface supporting a molecular layer of thickness dh is $dp = -g\rho dh$, where g is the gravitational acceleration and ρ the density of the layer. Replacing dp with the equation of a state of a perfect gas calculated for dry air, $dp = d\rho R\bar{T}/\bar{M}$, where R is the gas constant, \bar{M} is the mass of a mole of dry air and \bar{T} is the average temperature, and integrating, we find that in the first approximation the number density N_m of the

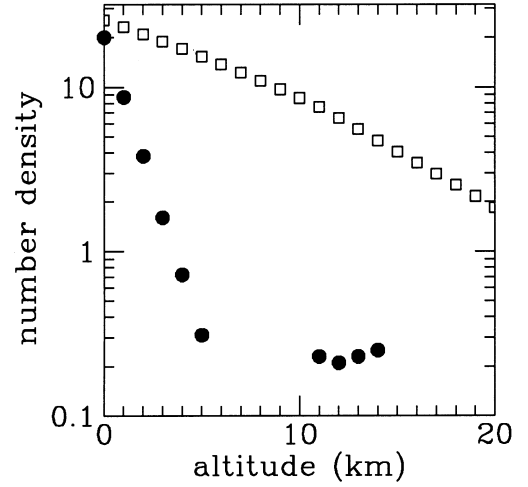


Figure 3. Examples of vertical distributions of molecules (squares) and haze aerosols (circles) in the atmosphere from respectively the US Standard Atmosphere (1962) and the Eltermann (1964) Clear Standard Atmosphere.

gaseous component of the atmosphere decreases exponentially with altitude h . If \bar{n} is the average number of molecules in a mole of dry air,

$$N_m(h) = \frac{\rho_0 \bar{n}}{\bar{M}} \exp\left(-\frac{\bar{M}g}{RT}h\right) = N_{m,0} e^{-ch}. \quad (10)$$

Measurements show that this is a good approximation for the first 10 km (see e.g. Fig. 3). We have adopted this simple model as did Garstang (1986), neglecting improvements carried out by Garstang (1991a) for higher altitudes. As did Garstang (1986), we have assumed an inverse scale altitude $c = 0.104 \text{ km}^{-1}$ and a molecular density at sea level $N_{m,0} = 2.55 \times 10^{19} \text{ cm}^{-3}$.

4.1.2 Haze aerosol vertical distribution

We are interested in average atmospheric conditions, better if typical and not in the particular conditions of a given night, so a detailed modelling of the local aerosol distribution in a given night is beyond the scope of this paper. As did Garstang (1986) and Joseph et al. (1991), we have assumed an exponential decrease of number density for the atmospheric haze aerosols:

$$N_a(h) = N_{a,0} e^{-ah}, \quad (11)$$

where h is the altitude and a is the inverse scale altitude. Measurements show (see e.g. Fig. 3) that for the first 10 km this is a reasonable approximation. To account for the presence of sporadic denser aerosol layers at various heights or at ground level as in Garstang (1991b) is beyond the scope of this work. We have also neglected the effects of the ozone layer and the presence of volcanic dust which have been studied by Garstang (1991a,c).

We take into account changes in aerosol content as in Garstang (1986), introducing a parameter K which measures the relative importance of aerosol and molecules for scattering of light in the V band:

$$K = \frac{N_{a,0} \sigma_a}{N_{m,0} \sigma_m 11.11 e^{-cH}}, \quad (12)$$

where H is the altitude above sea level of the ground level. Changing the parameter K , we are able to compute the map for different aerosol contents, i.e. for different products $N_a \sigma_a$. As in

Garstang (1986), the inverse scale altitude of aerosols is assumed to be $a = 0.657 + 0.059K$. Effects of changes of aerosol scale altitude are checked in Section 4.7.1. More detailed atmospheric models could be used whenever available.

4.2 Angular scattering functions

We take into account both Rayleigh scattering by molecules and Mie scattering by aerosols. For molecular Rayleigh scattering the angular scattering function is

$$f_m(\omega) = 3[1 + \cos^2(\omega)]/16\pi. \quad (13)$$

The integrated Rayleigh scattering cross-section in the *V* band is assumed to be $\sigma_m = 1.136 \times 10^{-26} \text{ cm}^2 \text{ sr}^{-1}$, and in the *B* band it is $\sigma_m = 4.6 \times 10^{-27} \text{ cm}^2 \text{ sr}^{-1}$.

The normalized angular scattering function for atmospheric haze aerosols can be measured easily with a number of well-known remote-sensing techniques like classical searchlight probing (see e.g. Eltermann 1966), modern bistatic lidar probing, measurements of the day-light or moonlight sky scattering function (see e.g. Hulburt 1951; Volz 1987; Krisciunas & Schaefer 1991). Nevertheless, in this paper we are interested not in a specific function for a given site at a given time, but in the typical average function, so we have adopted the function tabulated by McClatchey et al. (1978) as interpolated by Garstang (1991a), and we have neglected geographical gradients.

For $0^\circ \leq \omega \leq 10^\circ$,

$$f_a(\omega) = 7.5 \exp[-0.1249\omega^2/(1 + 0.04996\omega^2)].$$

For $10^\circ < \omega \leq 124^\circ$,

$$f_a(\omega) = 1.88 \exp(-0.07226\omega + 0.0002406\omega^2). \quad (14)$$

For $124^\circ < \omega \leq 180^\circ$,

$$f_a(\omega) = 0.025 + 0.015 \sin(2.25\omega - 369.0).$$

Here, ω is the scattering angle in degrees. The total integrated scattering cross-section $N_a\sigma_a$ is given by equation (12) for a given K . In the *B* band, σ_a is 1.216 times the value of the σ_a in the *V* band.

4.3 Upward emission function

The normalized emission function of each area gives the relative upward flux per unit solid angle in every direction. It is the sum of the direct emission from fixtures and the reflected emission from lighted surfaces, normalized to its integral, and is not known. The high number of sources contributing to the sky brightness of a site with random distribution and orientation smooth the shape of the average normalized emission function, which can be considered to a first approximation axisymmetric. It is possible to measure the average upward emission of a chosen area at a number of different elevation angles when a large number of satellite measurements from very different orbits are available. It will be possible to obtain it directly by integrating the upward emission from all lighting fixtures and all lighted surfaces on the basis of lighting engineering data and models, as soon they are available.

In this paper we have assumed that all land areas have the same average normalized emission function. This is equivalent to assuming that lighting habits are similar on average in each land area, and that differences from the average are randomly distributed in the territory. The average normalized emission function can be

constrained from radiance measurements of cities at various distances from the satellite nadir. It can also be obtained from comparison of Earth-based observations and model predictions (Cinzano, in preparation). We have chosen to assume this function and check its consistency with satellite measurements, rather than directly determine it from satellite measurements, because at very low elevation angles the spread is much too large to constrain the function shape adequately.

We have adopted for the average normalized emission function the normalized city emission function from Garstang (1986):

$$I(\psi) = \frac{1}{2\pi} [2a_1 \cos(\psi) + 0.554a_2\psi^4], \quad (15)$$

where a_1 and a_2 are shape parameters. Here we have assumed $a_1 = 0.46$ and $a_2 = 0.54$ for the typical average function, corresponding to Garstang parameters $G = 0.15$ and $F = 0.15$. This function was tested by Garstang with many comparisons between model predictions and measurements. He assumed this function to be produced by the sum of direct emission from fixtures at high zenith distances and Lambertian emission from lighted horizontal surfaces at lower zenith angles. Nevertheless, upward flux can be emitted at all zenith angles from both fixtures and vertical or horizontal surfaces, so we prefer to consider Garstang's function as a parametric representation with a_1 and a_2 as shape parameters without any meaning of fractions of direct and reflected light. We have also tested the normalized city emission function of Cinzano (2000b,c) which assumes a slightly higher emission at intermediate angles with respect to the function (15):

$$I(\psi) = \frac{1}{2\pi} (a_1 + 0.554a_2\psi^4), \quad (16)$$

assuming $a_1 = 0.79$ and $a_2 = 0.21$. Comparisons between these functions are presented by Cinzano (2000b).

We have checked these functions by studying the relation between the upward flux per unit solid angle per inhabitant of a large number of cities and their distance from the satellite nadir in a single-orbit satellite image taken on 1997 January 13 at 20:27 UT from satellite *FI2*, which was chosen for its large cloud-free area. Taking into account the average orbital distance R_S and the Earth curvature radius R_T , it is possible, with some geometry, to relate the distance D from satellite nadir with the emission angle ψ :

$$\psi = \frac{D}{R_T} \arcsin \frac{R_T \sin(D/R_T)}{s}, \quad (17)$$

with

$$s = \sqrt{R_T^2 + (R_T + R_S)^2 - 2R_T(R_T + R_S) \cos\left(\frac{D}{R_T}\right)}. \quad (18)$$

The flux per unit solid angle per inhabitant in relative units is obtained by dividing the measurements by the corresponding extinction coefficient $\xi_3(\psi)$ computed for a curved Earth from equation (20) of Garstang (1989a):

$$\xi_3 = \exp[-N_m\sigma_m(A1 + 11.778KA2)],$$

$$A1 = \frac{1}{c} \sec \psi \left(1 - e^{-c s \cos \psi} + \frac{16 \tan^2 \psi}{9\pi} \frac{1}{2cR_T} B1 \right),$$

$$B1 = (c^2 s^2 \cos^2 \psi + 2cs \cos \psi + 2) e^{-cs \cos \psi} - 2, \quad (19)$$

$$A2 = \frac{1}{a} \sec \psi \left(1 - e^{-as \cos \psi} + \frac{16 \tan^2 \psi}{9\pi} \frac{B2}{2aR_T} \right),$$

$$B2 = (a^2 s^2 \cos^2 \psi + 2as \cos \psi + 2) e^{-as \cos \psi} - 2.$$

Fig. 4 shows the relative flux per unit solid angle per inhabitant averaged over ranges of 100 km.

In Fig. 5 we show the $I(\psi)$ obtained with equations (17) and (19), compared with the Garstang (1986) function (solid line) and with the Cinzano (2000b) function (dashed line), with the assumed shape parameters. The fits are good with both. Error bars are not necessarily related to fluctuations in function shape, but rather to fluctuations in the total flux per inhabitant. Given that the extinction effects seems to balance the changes in measured flux at angles off-nadir (see Fig. 4), we did not need to correct the input images from single orbits for these off-nadir effects when computing the composite image.

Snow reflects approximately 60 per cent of downlight, changing the shape of the upward emission function. Lighted roads usually are cleared in a few days, so reflection of street lighting by snow on road surfaces is unlikely to be important, but reflection of the artificial sky light by snow on the rest of the land could noticeably

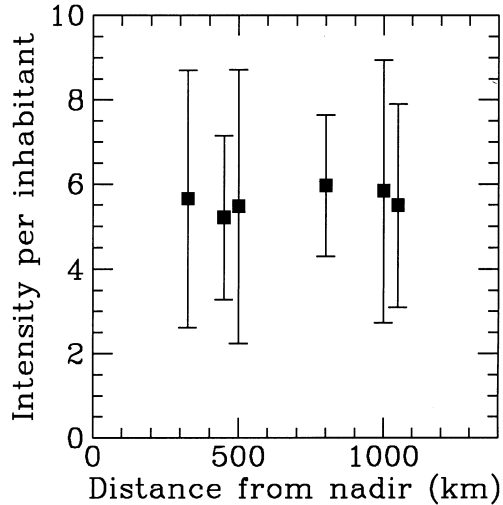


Figure 4. Relative flux per unit solid angle per inhabitant averaged over ranges of 100 km, measured for a sample of cities versus their distance from satellite nadir.

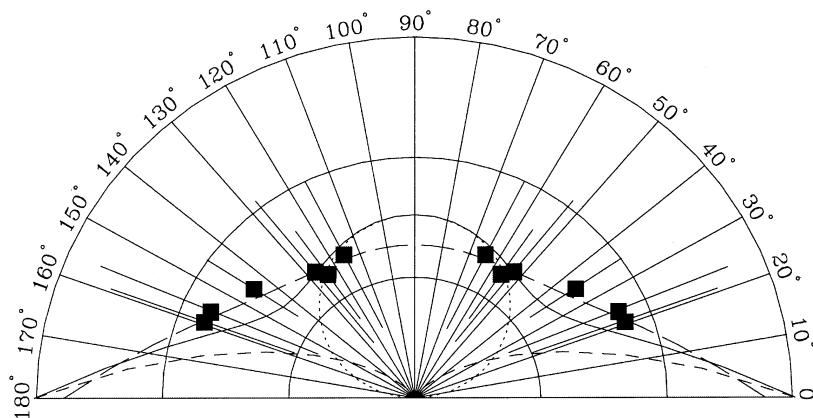


Figure 5. Average upward flux per unit solid angle per inhabitant compared with the Garstang upward emission function (solid line) and the Cinzano upward emission function (dashed line) for the adopted shape parameters. The components of the Garstang function are also shown (dotted and short-dashed lines).

enhance the upward flux in more polluted areas. Assuming roughly that 10 per cent of the upward flux is scattered downward by atmospheric particles and molecules, and that 60 per cent of it is reflected upward again by the snow-covered terrain, the increase of artificial sky brightness by snow reflection of sky light could reach 6 per cent. The upward flux owing snow reflection in some zones of Europe (our images are taken in winter) is likely detected by the OLS-PMT, but the different shape of the upward emission function could produce small errors. We plan to use specific satellite surveys to detect snow-covered areas where the upward emission function must be corrected. Even the offshore lights in the North Sea, where oil and gas production sites are active, could have a different upward emission function.

4.4 Geometric relations

In this paper we are more interested in understanding and comparing light pollution distributions in the European territory than in predicting the effective sky brightness for observational purposes, so we have computed the artificial sky brightness at sea level, in order to avoid introduction of altitude effects in our maps. We plan to take account of altitudes in a forthcoming paper devoted to mapping the naked-eye star visibility, which requires the computation of starlight extinction and natural sky brightness for the altitude of each land area.

With the hypothesis of sea level, geometrical relations from Garstang (1989a) between quantities shown in Fig. 6, taking into account Earth curvature, became simpler. They are listed in Appendix A. In equation (12) now $H = 0$. Equations (4) and (7) have been integrated by Garstang [1989a: equations (18), (19) and (22) and equations (20) and (21)]. They are listed in Appendix A too.

The correction for double scattering of Garstang (1989a) becomes

$$D_S = 1 + N_{m,0} \sigma_m \left(11.11 K f_2 + \frac{f_1}{3} \right), \quad (20)$$

where f_1 and f_2 are given in equation (A3). Integration of equation (3) must be done only where the curvature of Earth does not shield the line of sight from the source. We need to start integration from u_0 as given by [from equations (12) and (13) of Garstang (1989a)]

$$u_0 = \frac{2R_T \sin^2(D/2R_T)}{\sin z \cos \beta \sin(D/R_T) + \cos z \cos(D/R_T)}. \quad (21)$$

We have neglected the presence of mountains which might shield the light emitted from the sources from a fraction of the

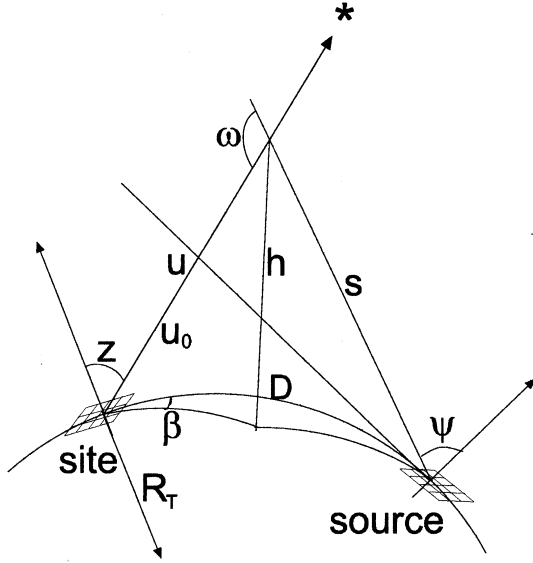


Figure 6. Geometrical relationships.

atmospheric particles along the line of sight of the observer. Assuming a flat Earth, mountains between source and observatory shield the light emitted from the source with an angle less than $\theta = \arctan(H/p)$ where H is the height of the mountain and p its distance from the source. The ratio between the luminance in the shielded and non-shielded cases is given, to first approximation, by the ratio between the numbers of particles illuminated in the two cases:

$$\frac{b_s}{b_{ns}} \approx \frac{\sigma_a f_a(\omega) \int_{Hq/p}^{\infty} N_a(h) dh + \sigma_m f_m(\omega) \int_{Hq/p}^{\infty} N_m(h) dh}{\sigma_a f_a(\omega) \int_0^{\infty} N_a(h) dh + \sigma_m f_m(\omega) \int_0^{\infty} N_m(h) dh}, \quad (22)$$

where q is the distance of the site from the source, $N_m(h)$ and $N_a(h)$ are respectively the vertical number densities of molecules and aerosols at the altitude h , σ_m and σ_a are their scattering sections and roughly $\omega \approx \pi - \theta$. This expression shows that, given the vertical extent of the atmosphere with respect to the height of the mountains, the shielding is not negligible only when the source is very near the mountain and both are quite far from the site (Garstang 1989a; see also Cinzano 2000c): $q/p \gg h_a/H$, where h_a is the vertical scaleheight of the atmospheric aerosols. This condition in the considered territories usually applies to poorly lighted areas only, which produce little pollution. The curvature of Earth emphasizes this behaviour.

4.5 Relation to atmospheric conditions

The adopted modelling technique allows us to assess the atmospheric conditions for which a map is computed, giving observable quantities like the vertical extinction at sea level in magnitudes (Garstang 1989a):

$$\Delta m = 1.0857 N_{m,0} \sigma_m \left[\left(\frac{550}{\lambda} \right)^4 \frac{1}{c} + \left(\frac{550}{\lambda} \right) \frac{11.778K}{a} \right], \quad (23)$$

where for the V band $\lambda = 550$ and for the B band $\lambda = 440$. Neglecting the curvature of Earth, the horizontal visibility, defined as the distance at which a black object would show a brightness of 0.98 of the brightness of the background horizon due to scattered

light, is (Garstang 1986)

$$\Delta x = \frac{3.91}{N_{m,0} \sigma_m} \left[\left(\frac{550}{\lambda} \right)^4 + 11.778K \left(\frac{550}{\lambda} \right) \right]^{-1}. \quad (24)$$

Effects of curvature have been discussed by the cited author. Other relations exist, with measurables like the Linke turbidity factor for total solar radiation received on the Earth (Garstang 1988). The optical thickness τ is [from equation (22) of Garstang 1986]

$$\tau = \Delta m / 1.0857. \quad (25)$$

With $K = 1$ we obtain $\tau = 0.3$, so the double-scattering approximation is adequate in our map computations. In order that $\tau \leq 0.5$ we need $K \leq 2.2$.

4.6 Spectral emission

DMSP satellites do not carry a spectrograph able to obtain spectra of the upward light emitted by each land area. However, it is possible to recover information about the spectral emission from the differential effects of extinction on light of different wavelengths. Calling $I(\lambda)$ the specific radiance of each land area at wavelength λ , $T(\lambda)$ the PMT sensitivity curve and $\xi_4(\lambda, K)$ the vertical extinction for a given clarity parameter K , the radiance $r(\lambda)$ measured by the OLS-PMT is

$$r(K) = \int_0^{\infty} T(\lambda) I(\lambda) \xi_4(\lambda, K) d\lambda. \quad (26)$$

The vertical extinction can be obtained from equation (23):

$$\xi_4(\lambda, K) = \exp(p_1 \lambda^{-4}) \exp(p_2 K \lambda^{-1}),$$

$$p_1 = -N_{m,0} \sigma_m \lambda_0^4 / c, \quad (27)$$

$$p_2 = -11.778 N_{m,0} \sigma_m \lambda_0 / a,$$

where the molecular scattering cross-section σ_m at $\lambda_0 = 550$ nm, the molecular density at sea level $N_{m,0}$ and the inverse scaleheights of molecules and aerosols c and a are given in Section 4.1. Equation (26) could be inverted with a Richardson–Lucy algorithm in order to recover $I(\lambda)$ from $r(K)$, a function which can be obtained by comparing many radiance-calibrated images obtained in different atmospheric conditions. The average clarity parameter K for each image can be obtained by comparing the variations of measured radiance with increasing distance from satellite nadir.

Fig. 7 shows in the lower panel the $r(K)$ curves produced by the example spectra $I(\lambda)$ in the upper panel. Curves have been scaled so that $r(K = 1) = 1$. Spectra with a similar effective wavelength after convolution with the PMT sensitivity curve, like e.g. a constant (dashed curve), a blackbody at 4000 K (dotted curve) and a narrow Gaussian centred at 650 nm (long-dashed curve), give almost the same $r(K)$ curve. However, spectra with lower or higher effective wavelength, like a Gaussian centred at 440 nm (dot-long-dashed curve), at 550 nm (solid curve) or at 800 nm (dot-dashed curve), give different $r(K)$ curves.

We have obtained the maps for the B and V photometric astronomical bands. The relative $B - V$ colour index of each land area could be inferred from the $r(K)$ curves, but requires some assumptions on the shape of the spectra. For simplicity in this paper we assumed it to be constant everywhere, and we only took into account the different propagation of the light in the

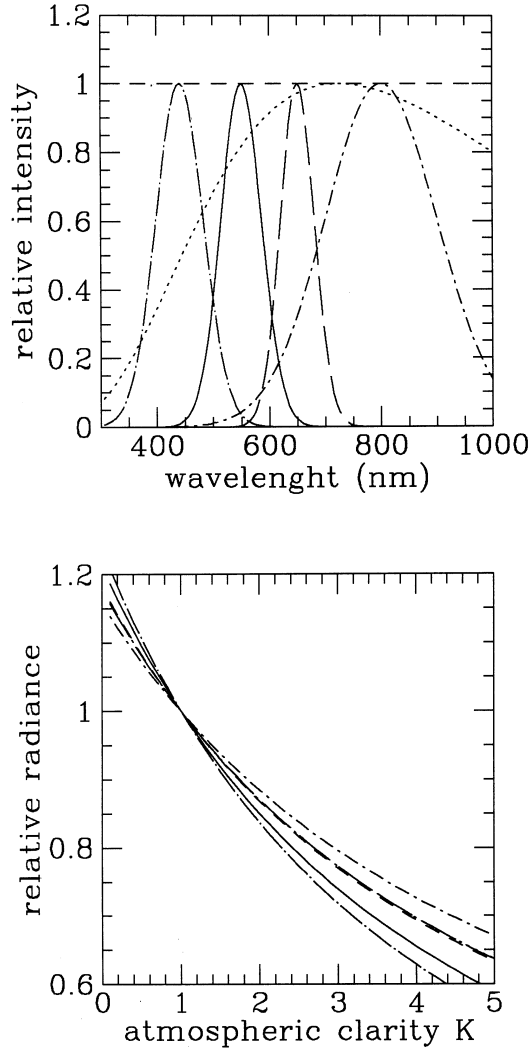


Figure 7. The $r(K)$ curves (lower panel) for some example spectra (upper panel). Spectra with a similar effective wavelength after convolution for the PMT sensitivity curve, like e.g. a constant (dashed curve), a blackbody at 4000 K (dotted curve) and a narrow Gaussian centred at 650 nm (long-dashed curve), give almost the same $r(K)$ curve. However, spectra with lower or higher effective wavelength, like a Gaussian centred at 550 nm (solid curve) or at 800 nm (dot-dashed curve), give $r(K)$ curves with respectively more or less pendency.

atmosphere in the two bands. We plan to study differences in city spectra in future work.

4.7 Calibration

We calibrated the maps on the basis of both (i) accurate measurements of sky brightness together with extinction from the Earth's surface and (ii) analysis of before-fly radiance calibration of OLS-PMT.

4.7.1 Calibration with Earth-based measurements

A detailed calibration requires sky brightness measurements at a large number of sites at sea level, taken on nights with the same vertical extinction and horizontal visibility of the map under calibration, averaged over many nights in order to smooth

atmospheric fluctuations. Observations need to be *under the atmosphere*, i.e. as actually observed from the ground without any extinction correction applied. To obtain the artificial sky brightness it would be necessary to measure the natural sky brightness at some sites where the maps suggest that the artificial one is negligible, and subtract the mean from all measurements. Moreover, given the fast growth rate of artificial sky brightness, which in Italy, for example, reaches 10 per cent per year (Cinzano 2000d), measurements have to be taken in the same period and the calibration will refer to that time.

Measurements of sky brightness in Europe in the V and B bands in the period 1996–99 are scarce, so we calibrated our maps with all available measurements in the chosen bands taken in 1998 and in 1999 on clean or photometric nights, even if extinction was not available or not exactly the required one (Della Prugna 1999; Catanzaro & Catalano 2000; Cinzano 2000d; Favero et al. 2000; Piersimoni, Di Paolantonio & Brocato 2000; Poretti & Scardia 2000; Zitelli 2000). Some data have been taken by one of us for this purpose with a small portable telescope and a CCD device (Falchi 1998). Most of the sites are at sea level but we also included a few sites at altitudes under 1300 m above sea level. Because of lack of measurements of natural sky brightness in Europe at sea level, we assumed it to be, at minimum solar activity, $B = 22.7 \text{ mag arcsec}^{-1}$ in the B band, and $V = 21.6 \text{ mag arcsec}^{-1}$ in the V band, estimating an uncertainty of at least $\pm 0.1 \text{ mag arcsec}^{-1}$. Natural sky brightness increases when solar activity increases (Walker 1988), and the solar activity in 1998 was close to the minimum but not at the minimum, so it could be underestimated and consequently the artificial brightness in darker sites considerably overestimated. The sky brightness has been transformed into photon radiance with the formulae of Garstang [1989a: equations (28) and (39)].

A least-squares fit of a straight line $y = a + x$ over the logarithmic measured radiances versus the logarithmic predicted radiances gives the logarithmic calibration coefficients $a_B = -0.63 \pm 0.04$ and $a_V = 0.00 \pm 0.04$. We assumed to be unavailable the uncertainties of measurements as given by atmospheric conditions and emission function fluctuations. The uncertainty of the calibration coefficients produces an uncertainty of about 10 per cent in the calibrated predicted radiances. However, single data points show differences of as much as about 60 per cent, so that we consider it safer to assume this last value as an estimate of the uncertainty of our calibrated predictions for a given site. More precise calibrations will be possible when a large number of measurements of sky brightness at sea level together with extinction become available. A large CCD measurement campaign is being set up.

In Figs 8 and 9 we have compared our calibrated predictions with the available measurements of artificial sky brightness respectively in the V and B bands. Photon radiance in the V band is expressed in units of $0.3419 \times 10^{10} \text{ photon s}^{-1} \text{ m}^{-2} \text{ sr}^{-1}$, corresponding approximately to a luminance of one $\mu\text{cd m}^{-2}$, and in the B band in units of $10^{10} \text{ photon s}^{-1} \text{ m}^{-2} \text{ sr}^{-1}$. Error bars indicate measurement errors which are much smaller than the effects of fluctuations in atmospheric conditions.

We have checked the effects on the predictions of Figs 8 and 9 of changes of (i) atmospheric conditions and (ii) the shape of $I(\psi)$. An increase of the aerosol content parameter K increases the extinction exponentially and the scattering linearly along the line of sight, so that, excluding a small area very near the source where the extinction is negligible, the predicted artificial sky brightness decreases everywhere: a well-known result (Garstang 1986,

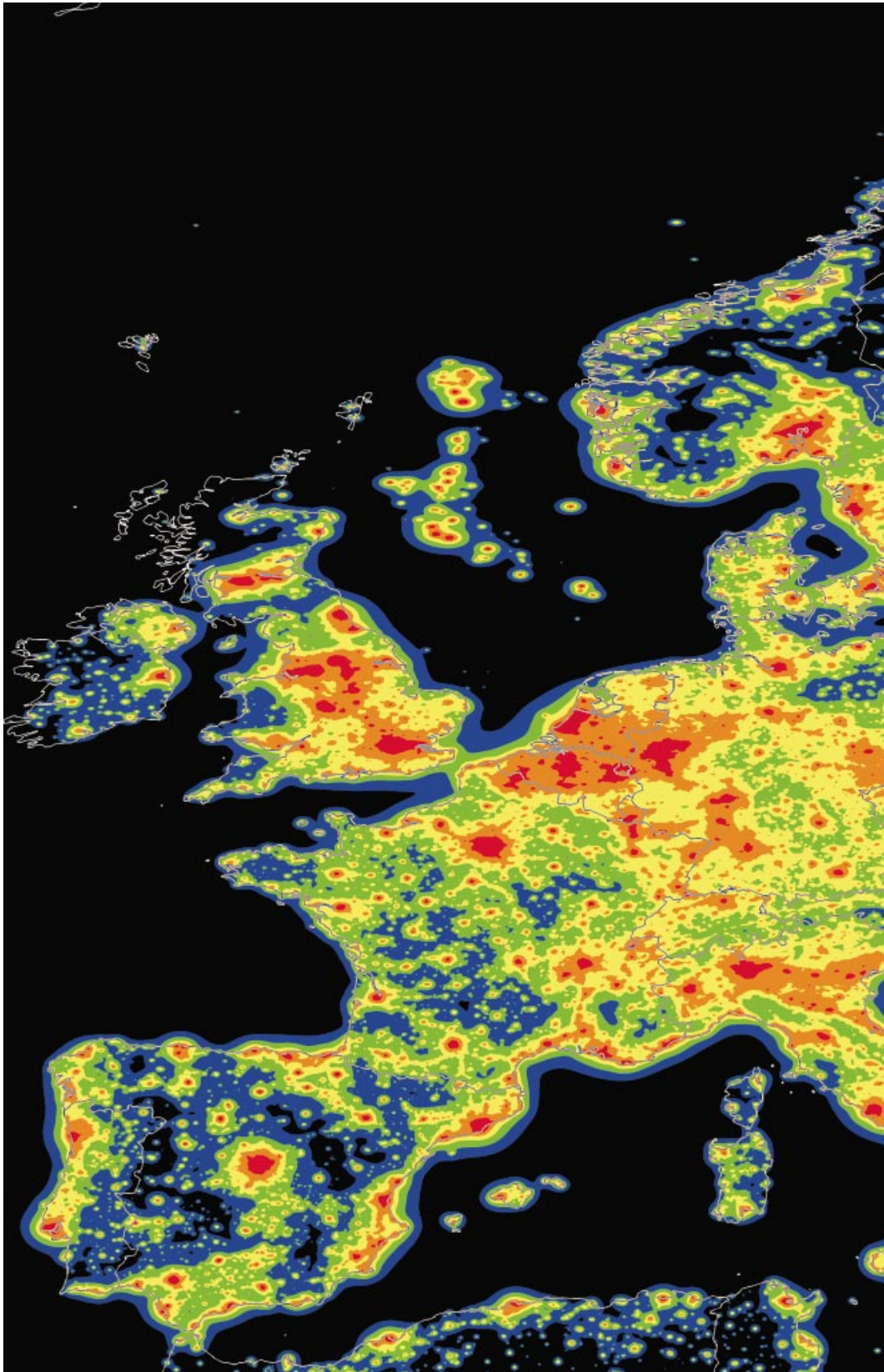


Figure 11. Artificial sky brightness at sea level in Europe in the V band for aerosol content parameter $K = 1$ (part one).

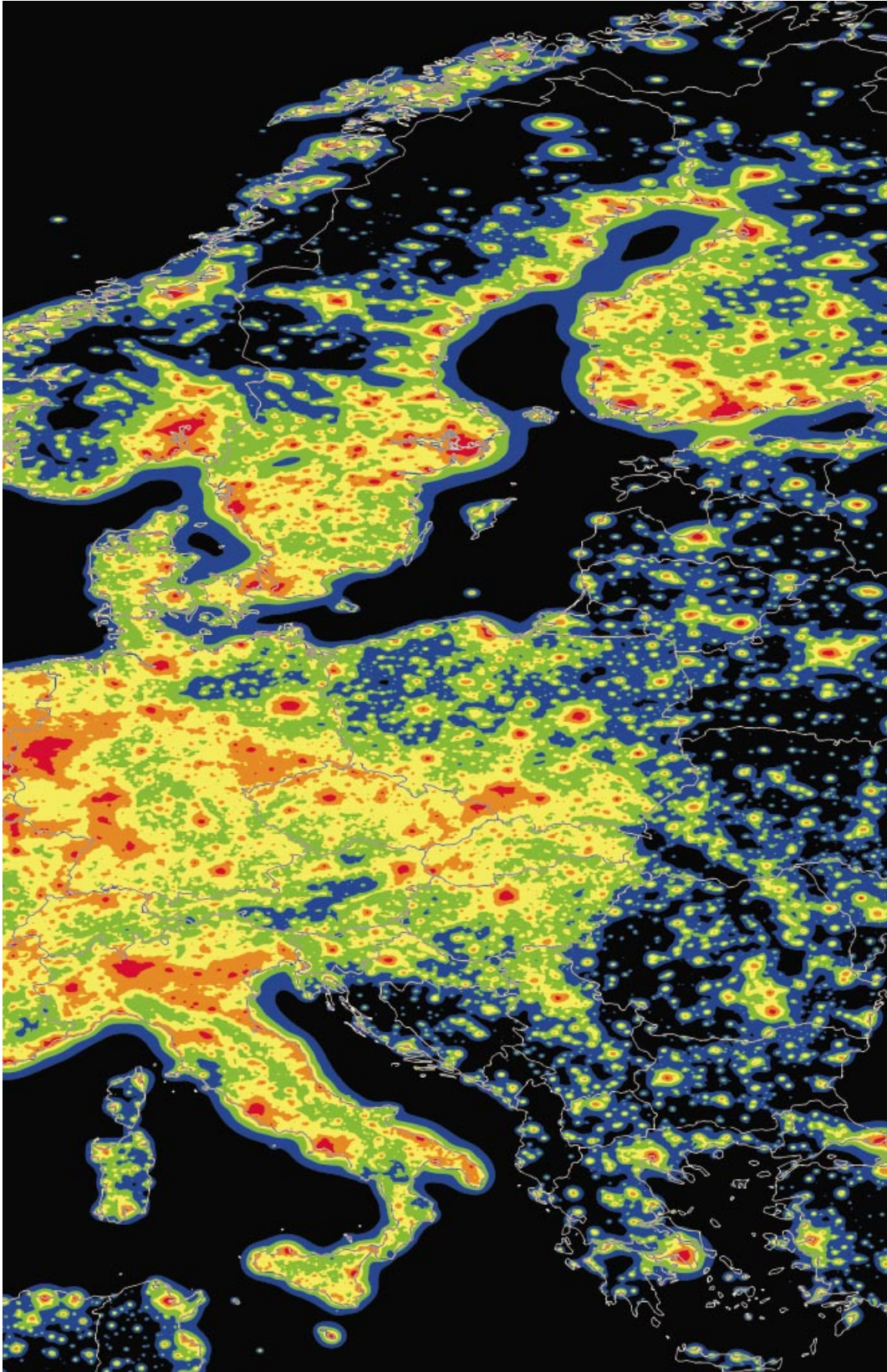


Figure 12. Artificial sky brightness at sea level in Europe in the V band for aerosol content parameter $K = 1$ (part two).

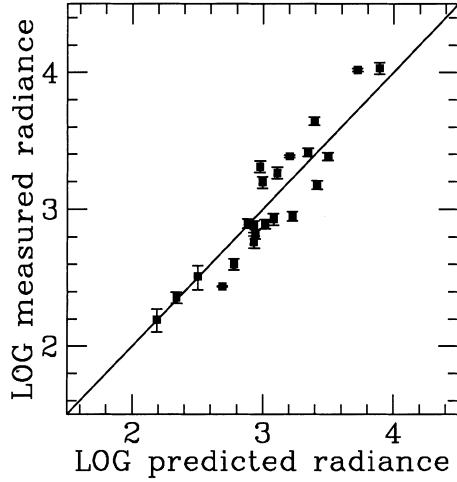


Figure 8. Measurements of artificial sky brightness versus calibrated map predictions in the V band.

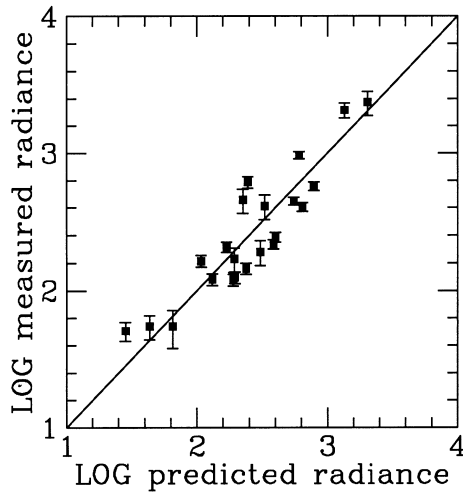


Figure 9. Measurements of artificial sky brightness versus calibrated map predictions in the B band.

1989a, 2000; Cinzano 2000c). The decrease is larger for areas farther from sources. These usually are darker, so, in the log–log diagram, with increasing haze, darker sites move toward low predicted brightness more than less dark sites. A change of aerosol scalelength has a similar effect. A change of the shape of the upward emission function $I(\psi)$ has a different effect. Decreasing the relative emission at low elevations (large ψ), the sky brightness is decreased approximately proportionally at almost all sites, except very near the source (see also Cinzano & Diaz Castro 2000), so in a log–log diagram all sites move toward a low predicted brightness of nearly the same quantity. This opens the way to detecting cities with more light-wasting installations. In fact, if a series of measurements of sky brightness at increasing distance from a city lies on a straight line parallel to the calibration line but displaced toward lower predicted values, probably the relative emission of the city at low elevation is higher than assumed in making the map. This is a typical result of street lights that are poorly shielded or too much inclined.

Shifts in measurements obtained with different instrumental setups could arise because, as shown in Fig. 10, the average emission spectrum has typically its maximum to one side of the

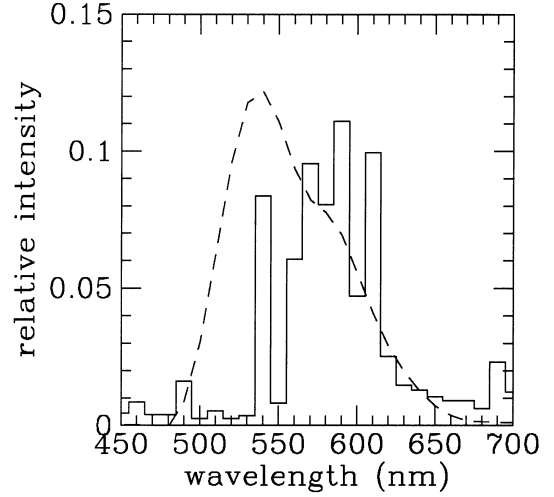


Figure 10. The composite spectrum of upward emission (solid line) used for checking the consistency of Earth-based map calibration with PMT radiance calibration. We roughly assumed 50 per cent of the total power produced by HPS lamps and 50 per cent by Hg vapour lamps. Dashed line shows the V band sensitivity curve.

V-band sensitivity curve, so that the resulting measurements are quite sensitive to small differences between the instrumental curve and the standard V-band curve.

4.7.2 Calibration with pre-fly irradiance measurements

Map calibration based on pre-fly irradiance calibration of OLS-PMT requires the knowledge, for each land area (i, j) , of (i) the average vertical extinction Δm during satellite observations and (ii) the relation between the radiance in the chosen photometric band and the radiance measured in the PMT spectral sensitivity range, which depends on the emission spectra. Both of them are unknown.

If \bar{r} is the energetic radiance in units of $10^{10} \text{ W cm}^{-2} \text{ sr}^{-1}$, the upward energy flux in W in the PMT photometric band is

$$e(i, j) = \bar{r}(i, j) \frac{A(i, j)}{I(\psi = 0)} 10^{0.4\Delta m}, \quad (28)$$

where $I(\psi)$ is the upward emission function and A is the surface area in km^2 of the land area (i, j) :

$$A(i, j) = \left(\frac{2\pi\Delta x}{360 \times 60 \times 60} R_T \right)^2 \cos(l), \quad (29)$$

with l the latitude of the land area, R_T the average Earth radius in km and Δx the pixel size in arcsec.

The photon radiance in the V photometric band corresponding to the energetic radiance measured by the PMT is

$$\begin{aligned} \bar{f}_r(i, j) &= \frac{\int_0^\infty T_V(\lambda) I(\lambda) \frac{\lambda}{hc} d\lambda}{\int_0^\infty T_{\text{PMT}}(\lambda) I(\lambda) \frac{\lambda}{hc} d\lambda} \frac{\int_0^\infty T_{\text{PMT}}(\lambda) S(\lambda) \frac{\lambda}{hc} d\lambda}{\int_0^\infty T_{\text{PMT}}(\lambda) S(\lambda) d\lambda} \bar{r}(i, j) \\ &= \frac{\int_0^\infty T_V(\lambda) I(\lambda) \frac{\lambda}{hc} d\lambda}{\int_0^\infty T_{\text{PMT}}(\lambda) I(\lambda) \frac{\lambda}{hc} d\lambda} \langle \lambda \rangle \bar{r}(i, j), \end{aligned} \quad (30)$$

where T_V and T_{PMT} are the sensitivity curves respectively of the V

band and the PMT detector, $I(\lambda)$ is the energy spectrum of the emission from the chosen land area, $S(\lambda)$ is the energy spectrum of the pre-fly calibration source, h is Planck's constant and c is the velocity of light. The second ratio is the effective wavelength $\langle\lambda\rangle$ of the combination of the sensitivity curves of the PMT and the calibration source, divided by hc .

In order to check the consistency of our Earth-based V -band calibration with pre-fly radiance calibration of PMT images, we have obtained a tentative map calibration assuming for all land areas an average vertical extinction $\Delta m = 0.3$ mag in V at sea level, and constructing a synthetic spectrum for typical night-time lighting. We have very roughly assumed that 50 per cent of the total power emitted by each land area be produced by High Pressure Sodium (HPS) lamps (SON standard) and 50 per cent by Hg vapour lamps (HQL). The composite spectrum is visible in Fig. 10 (solid line), together with the V band (dashed line). The result of integration of equation (30) is $\bar{f}_r/\bar{r} \approx 1.48 \times 10^{18}$ photon $s^{-1} W^{-1}$, much less than the photon flux per unit power at 550 nm, $\sim 2.79 \times 10^{18}$ photon $s^{-1} W^{-1}$. Equations (28) and (30), taking in account the internal constants of the program and omitting the $\cos(l)$ already included in it, give the V -band logarithmic calibration coefficient $a_V = -0.01$. In spite of the uncertainties both in the extinction and in the average emission spectrum, this calibration agrees very well with the Earth-based calibration.

5 RESULTS

Figs 11, 12, 13 and 14 show the artificial sky brightness in Europe at sea level in the V and B bands. Colours correspond to ratios between the artificial sky brightness and the natural sky brightness of <0.11 (black), $0.11-0.33$ (blue), $0.33-1$ (green), $1-3$ (yellow), $3-9$ (orange), and >9 (red). Original maps are 4800×4800 pixel images saved in 16-bit standard FITS format with FITSIO FORTRAN 77 routines developed by HEASARC at the NASA Goddard Space Flight Center. Images have been analysed with the FTOOLS 4.2 analysis package by HEASARC and with QUANTUM IMAGE 3.6 by Aragon System.² Maps have been computed for a clean atmosphere with aerosol clarity $K = 1$, corresponding to a vertical extinction of $\Delta m = 0.33$ mag in the V band and $\Delta m = 0.56$ mag in the B band, horizontal visibility $\Delta x = 26$ km, and optical depth $\tau = 0.3$. We have limited our computations to zenith sky brightness even though our method allows determinations of brightness in other directions. This would be useful to predict visibility in large territories of particular astronomical phenomena, such as, e.g., comets. A complete mapping of the artificial brightness of the sky of a site, as in Cinzano (2000c), using satellite data instead of population data is possible (Cinzano, in preparation). Falchi & Cinzano (2000) and Cinzano et al. (2000) obtained in 1998 the first maps of the artificial sky brightness from satellite data using a DMSP single-orbit image and replacing f in equation (1) with the Treanor Law, a semi-empirical law which assumes a very simplified model with homogeneous atmosphere, vertical heights small in relation to the horizontal distances, scattering limited to a cone of small angle co-axial with the direct beam, and a flat earth. Differences from our maps mainly arise where the curvature of Earth plays a role in limiting the propagation of light pollution. Our study constitutes the natural improvement of their seminal work.

Recommendation 1 of the IAU Commission 50 (Smith 1979) states that the increase in sky brightness at 45° elevation owing to artificial light scattered from clear sky should not exceed 10 per

cent of the lowest natural level in any part of the spectrum between wavelengths 3000 and 10000 Å. So this is the level over which the sky must be considered 'polluted'. The maps shows that only a few areas in Europe are under the limit of 10 per cent at zenith, and some of them could still be quite polluted at higher zenith distances.

6 CONCLUSIONS

We have presented a method to map the artificial sky brightness in large territories in astronomical photometric bands with a resolution of approximately 1 km. We have computed the maps with detailed models for the propagation in the atmosphere of the upward light flux measured with the DMSP satellite Operational Linescan System. The use of this modelling technique allows us to (i) assess the atmospheric conditions for which the maps are computed, giving observable quantities, and (ii) take into account the curvature of Earth. This cannot be done properly when using semi-empirical propagation laws. The use of satellite data constitutes an improvement over the use of population data to estimate upward flux, because (i) it allows spatially explicit detail of the geographic distribution of emissions, and (ii) some polluting sources, such as industrial areas, ports and airports, are not well represented in population data.

We have presented, as an application of the described method, maps of artificial sky brightness in Europe at sea level in the V and B bands. We are extending the maps to the rest of the world in a forthcoming World Atlas of Artificial Sky Brightness, and preparing predictions for the state of the night sky in future years.

ACKNOWLEDGMENTS

We are indebted to Roy Garstang of JILA, University of Colorado, for his kindness in reading and commenting on this paper, for his helpful suggestions and for interesting discussions.

REFERENCES

- Abramowitz M., Stegun I. A., 1964, Handbook of Mathematical Functions. NBS, Washington
- Albers S., 1998, <http://laps.fsl.noaa.gov/albers/slides/ast/places.html>
- Berry R., J. R., 1976, Astron. Soc. Can., 70, 97
- Bertiau F. C. S. J., de Graeve E. S. J., Treanor P. J. S. J., 1973, Vatican Obs. Publ., 1, 4, 159
- Catanzaro G., Catalano F. A., 2000, in Cinzano P., ed., Measuring and Modelling Light Pollution. Mem. Soc. Astron. Ital., 71, 211
- Cinzano P., 1994, References on Light Pollution and Related Fields, v.2, Internal Rep. 11, Department of Astronomy, Padova (also on-line at <http://www.pd.astro.it/cinzano/refer/index.htm>)
- Cinzano P., 2000a, Measuring and Modelling Light Pollution. Mem. Soc. Astron. Ital., 71
- Cinzano P., 2000b, in Cinzano P., ed., Measuring and Modelling Light Pollution. Mem. Soc. Astron. Ital., 71, 93,
- Cinzano P., 2000c, in Cinzano P., ed., Measuring and Modelling Light Pollution. Mem. Soc. Astron. Ital., 71, 113
- Cinzano P., 2000d, in Cinzano P., ed., Measuring and Modelling Light Pollution. Mem. Soc. Astron. Ital., 71, 159
- Cinzano P., Diaz Castro F. J., 2000, in Cinzano P., ed., Measuring and Modelling Light Pollution. Mem. Soc. Astron. Ital., 71, 251
- Cinzano P., Falchi F., Elvidge C. D., Baugh K. E., 2000, Mem. Soc. Astron. Ital., in press
- Crawford D. L., 1991, Proc. Light Pollution, Radio Interference and Space Debris, ASP Conf. Ser., Vol. 17. Astron. Soc. Pac., San Francisco

² Aragon System, Tjalmargatan 6, 831 45 Ostersund, Sweden.

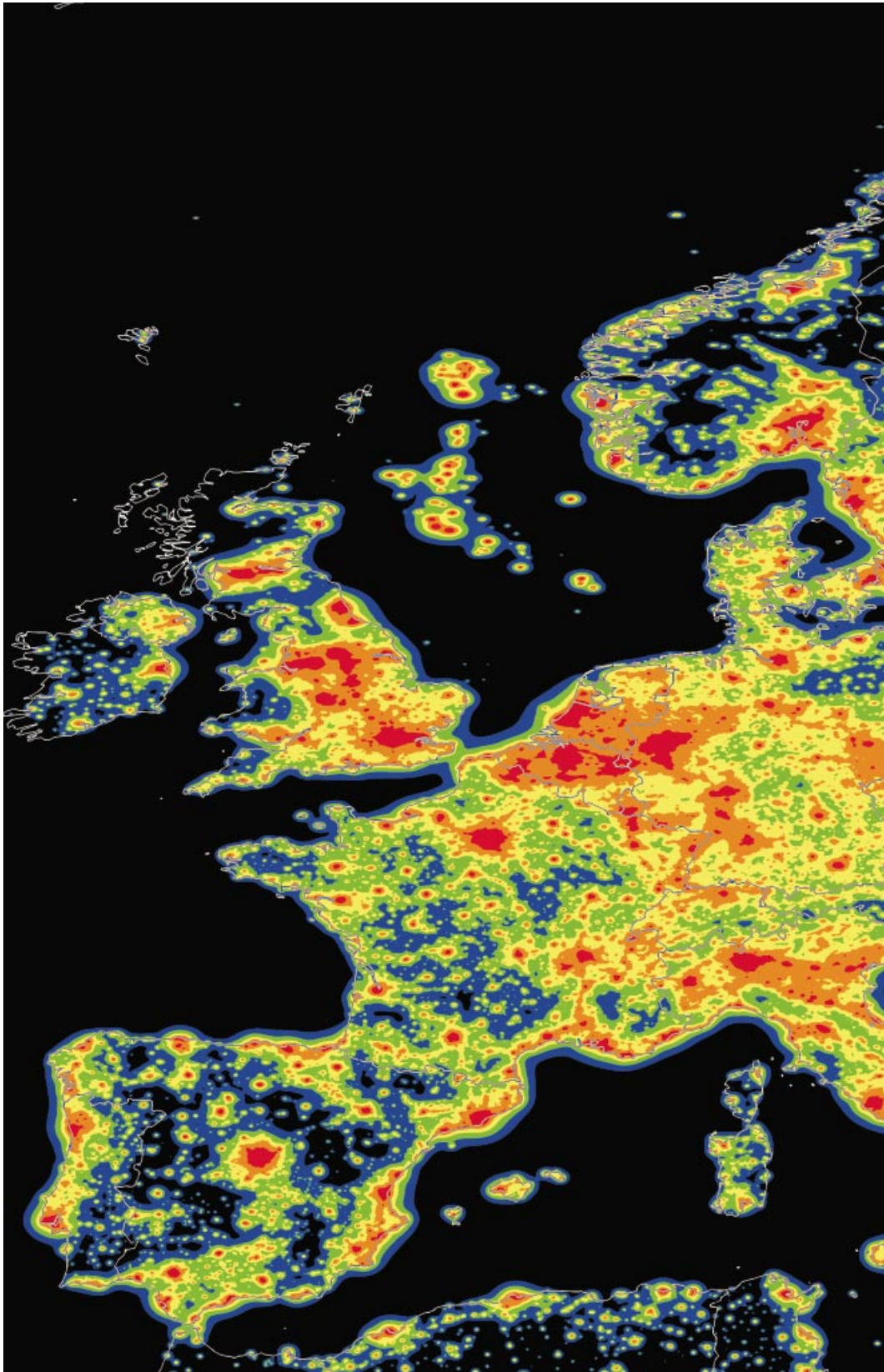


Figure 13. Artificial sky brightness at sea level in Europe in the *B* band for aerosol content parameter $K = 1$ (part one).

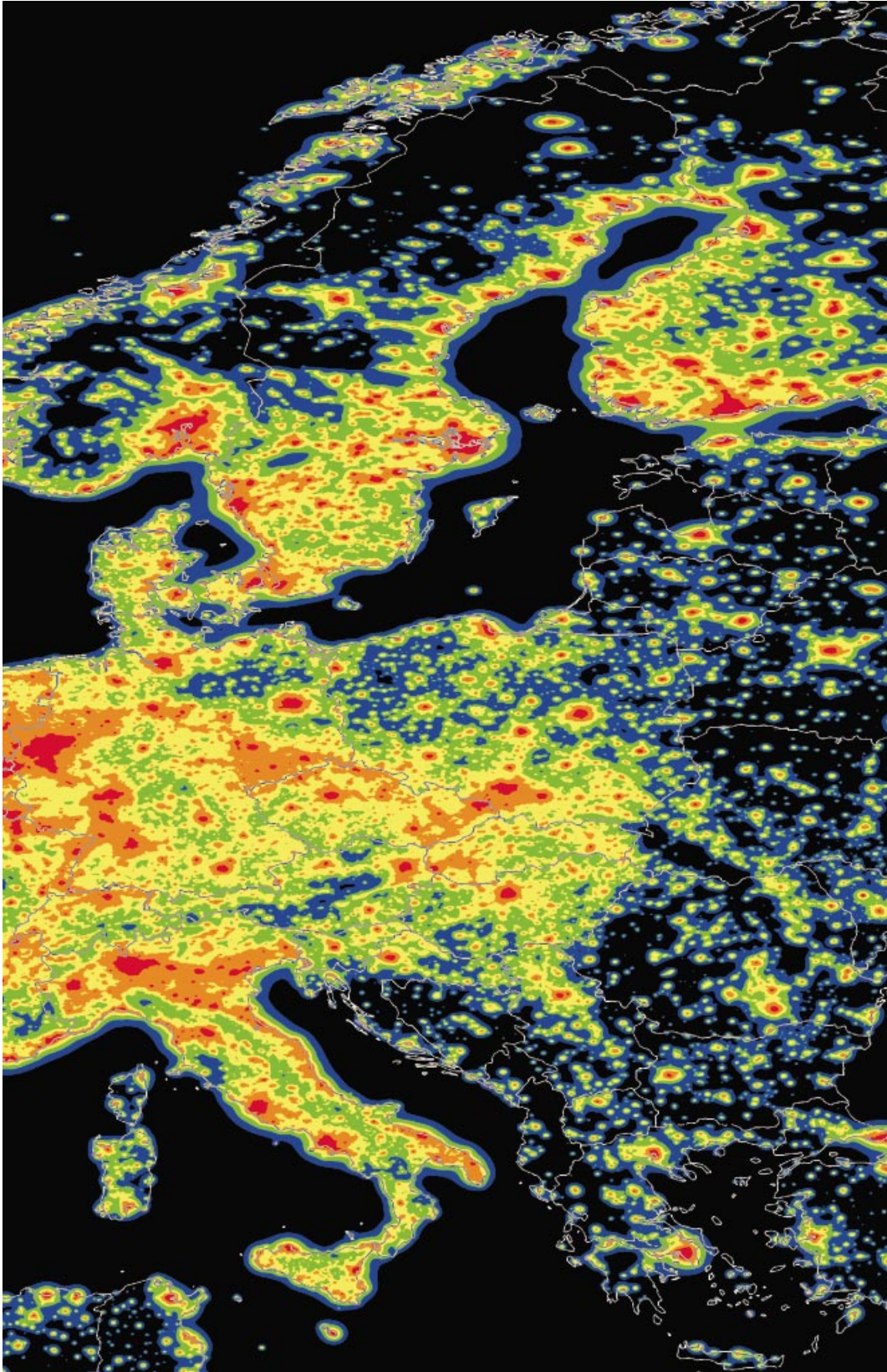


Figure 14. Artificial sky brightness at sea level in Europe in the B band for aerosol content parameter $K = 1$ (part two).

- Della Prugna F., 1999, *A&AS*, 140, 345
- Eltermann L., 1964, *Appl. Opt.*, 3, 6, 745
- Eltermann L., 1966, *Appl. Opt.*, 5, 11, 1769
- Elvidge C. D., Baugh K. E., Kihn E. A., Kroehl H. W., Davis E. R., 1997a, *Photogram. Eng. Remote Sens.*, 63, 727
- Elvidge C. D., Baugh K. E., Kihn E. A., Kroehl H. W., Davis E. R., Davis C., 1997b, *Int. J. Remote Sens.*, 18, 1373
- Elvidge C. D., Baugh K. E., Hobson V. H., Kihn E. A., Kroehl H. W., Davis E. R., Cocero D., 1997c, *Global Change Biol.*, 3, 387
- Elvidge C. D., Baugh K. E., Dietz J. B., Bland T., Sutton P. C., Kroehl H. W., 1999, *Remote Sens. Environ.*, 68, 77
- Falchi F., 1998, thesis, Univ. Milan
- Falchi F., Cinzano P., 2000, in Cinzano P., ed., *Measuring and Modelling Light Pollution*. *Mem. Soc. Astron. Ital.*, 71, 139
- Favero G., Federici A., Blanco A. R., Stagni R., 2000, in Cinzano P., ed., *Measuring and Modelling Light Pollution*. *Mem. Soc. Astron. Ital.*, 71, 223
- Garstang R. H., 1984, *Observatory*, 104, 196
- Garstang R. H., 1986, *PASP*, 98, 364
- Garstang R. H., 1987, in Millis R. L., Franz O. G., Ables H. D., Dahn C. C., eds, *Identification, optimization and protection of optical observatory sites*. Lowell Observatory, Flagstaff, p. 199
- Garstang R. H., 1988, *Observatory*, 108, 159
- Garstang R. H., 1989a, *PASP*, 101, 306
- Garstang R. H., 1989b, *ARA&A*, 27, 19
- Garstang R. H., 1989c, *BAAS*, 21, 2, 759
- Garstang R. H., 1991a, *PASP*, 103, 1109
- Garstang R. H., 1999b, in Crawford D. L., eds, *Proc. IAU Colloq. 112, Light Pollution, Radio Interference and Space Debris*, ASP Conf. Ser., Vol. 17. *Astron. Soc. Pac.*, San Francisco, p. 69
- Garstang R. H., 1991c, *Observatory*, 111, 239
- Garstang R. H., 1992, *BAAS*, 24, 740
- Garstang R. H., 1993, *BAAS*, 25, 1306
- Garstang R. H., 2000, in Cinzano P., ed., *Measuring and Modelling Light Pollution*. *Mem. Soc. Astron. Ital.*, 71, 71
- Goode J. P., 1925, *Assoc. Am. Geog. Ann.*, 115, 119
- Hulburt E. O., 1951, *J. Opt. Soc. Am.*, 31, 467
- Imhoff M. L., Lawrence W. T., Elvidge C. D., Paul T., Levine E., Prevalsky M., Brown V., 1997a, *Remote Sens. Environ.*, 59, 105
- Imhoff M. L., Lawrence W. T., Stutzer D. C., Elvidge C. D., 1997b, *Remote Sens. Environ.*, 61, 361
- Isobe S., Hamamura S., 1998, in Isobe S., Hirayama T., eds, *Proc. IAU JD5, Preserving the Astronomical Windows*, ASP Conf. Ser., Vol. 139. *Astron. Soc. Pac.*, San Francisco, p. 191
- Isobe S., Hirayama T., 1998, *Proc. IAU JD5, Preserving the Astronomical Windows*, ASP Conf. Ser., Vol. 139, *Astron. Soc. Pac.*, San Francisco
- Johnson H., 1955, *Ann. Astrophysics*, 18, 292
- Joseph J. H., Kaufman Y. J., Mekler Y., 1991, *Appl. Opt.*, 30, 3047
- Kovalevsky J., 1992, *The Protection of Astronomical and Geophysical Sites*, NATO Pilot Study No. 189. Editions Frontières, Paris
- Krisciunas K., Schaefer B. E., 1991, *PASP*, 103, 1033
- Lieske R. W., 1981, *Proc. Int. Telemetry Conf. vol. 17, International Foundation for Telemetry (IFT)*, Woodland Hills, CA, USA, p. 1013
- McClatchey R. A., Fenn R. W., Selby J. E. A., Volz F. E., Garing J. S., 1978, in Driscoll W. G., Vaughan W., eds, *Handbook of Optics*. McGraw-Hill, New York, Section 14
- McNally D., 1994, *Proc. IAU-ICSU-UNESCO Meeting on Adverse Environmental Impacts on Astronomy, The Vanishing Universe*. Cambridge Univ. Press, Cambridge
- Piersimoni A., Di Paolantonio A., Brocato E., 2000, in Cinzano P., ed., *Measuring and Modelling Light Pollution*. *Mem. Soc. Astron. Ital.*, 71, 221
- Pike R., J R., 1976, *Astron. Soc. Can.*, 70, 116
- Poretti E., Scardia M., 2000, in Cinzano P., ed., *Measuring and Modelling Light Pollution*. *Mem. Soc. Astron. Ital.*, 17, 203
- Smith F. G., 1979, *Rep. Astron.*, IAU Trans., XVIII, 218
- Steinwand D. R., 1993, *Int. J. Remote Sens.*, 15, 3463
- Sullivan W. T., 1989, *Int. J. Remote Sens.*, 10, 1
- Sullivan W. T., 1991, in Crawford D. L., *Proc. IAU Colloq. 112, Light Pollution, Radio Interference and Space Debris*, ASP Conf. Ser., Vol. 17. p. 11
- Sutton P., Roberts D., Elvidge C., Meij H., 1997, *Photogram. Eng. Remote Sens.*, 63, 1303
- Treanor P. J. S. J., 1973, *Observatory*, 93, 117
- Twomey S., 1977, *Atmospheric Aerosols*. Elsevier, Amsterdam
- US Standard Atmosphere, 1962, US Government Printing Office, Washington, DC
- Volz F. E., 1987, *Appl. Opt.*, 26, 4098
- Walker M. F., 1970, *PASP*, 82, 672
- Walker M. F., 1973, *PASP*, 85, 508
- Walker M. F., 1977, *PASP*, 89, 405
- Walker M. F., 1988, *PASP*, 100, 496
- Zitelli V., 2000, in Cinzano P., ed., *Measuring and Modelling Light Pollution*. *Mem. Soc. Astron. Ital.*, 71, 193

APPENDIX A: GEOMETRICAL RELATIONS

With the assumption of sea level, the geometrical relations from Garstang (1989a) between quantities in Fig. 6 become

$$s = \sqrt{(u - l)^2 + 4ul \sin^2(D/2R_T)}$$

with

$$l = \sqrt{4R_T^2 \sin^2(D/2R_T)},$$

$$h = R_T \left(\sqrt{1 + \frac{u^2 + 2uR_T \cos(z)}{R_T^2}} - 1 \right),$$

$$\omega = \theta + \phi \tag{A1}$$

with

$$\theta = \arccos \left[\frac{q_1}{\sqrt{4R_T^2 \sin^2(D/2R_T)}} \right],$$

$$\phi = \arccos \left(\frac{l^2 + s^2 - u^2}{2ls} \right),$$

$$\psi = \arccos \left(\frac{q_2}{s} \right),$$

$$q_1 = R_T [\sin(D/R_T) \sin(z) \cos(\beta) + \cos(D/R_T) \cos(z)]$$

$$q_2 = u \sin(z) \cos(\beta) \sin(D/R_T) + q_3,$$

$$q_3 = u \cos(z) \cos(D/R_T) - 2R_T \sin^2(D/2R_T),$$

where R_T is the curvature radius of the Earth.

Equations (4) and (7) have been integrated by Garstang [1989a: equations (18), (19) and (22), and (20) and (21)]. For sea level and $z < 90^\circ$ and $\psi < 90^\circ$, they are

$$\xi_1 = \exp[-N_{m,0} \sigma_m (p_1 + 11.778 K p_2)]$$

$$p_1 = c^{-1} \sec z \left[1 - \exp(-cu \cos z) + \frac{16p_3 \tan^2 z}{9\pi^2 c R_T} \right],$$

$$p_2 = a^{-1} \sec z \left[1 - \exp(-au \cos z) + \frac{16p_4 \tan^2 z}{9\pi^2 a R_T} \right], \tag{A2}$$

$$p_3 = (c^2 u^2 \cos^2 z + 2cu \cos z + 2) \exp(-cu \cos z) - 2,$$

$$p_4 = (a^2 u^2 \cos^2 z + 2au \cos z + 2) \exp(-au \cos z) - 2,$$

$$\xi_2 = \exp[-N_{m,0} \sigma_m (f_1 + 11.778 K f_2)],$$

Table B1. Orbits of satellite *F12*.

| | | |
|--------------|--------------|--------------|
| 199603191827 | 199702061858 | 199701091752 |
| 199603192009 | 199702062040 | 199701091934 |
| 199603192151 | 199702062222 | 199701092116 |
| 199603211803 | 199702081833 | 199701111727 |
| 199603211945 | 199702082015 | 199701111909 |
| 199603212127 | 199702082157 | 199701112051 |
| 199603231738 | 199702101809 | 199701131703 |
| 199603231920 | 199702101951 | 199701131845 |
| 199603232102 | 199702102133 | 199701132027 |
| 199701061828 | 199603171709 | 199701132209 |
| 199701062010 | 199603171851 | 199702031752 |
| 199701062152 | 199603172215 | 199702031934 |
| 199701081804 | 199603181839 | 199702032116 |
| 199701081946 | 199603182021 | 199702032258 |
| 199701082128 | 199603182203 | 199702051728 |
| 199701101740 | 199603201815 | 199702051910 |
| 199701101922 | 199603201957 | 199702052052 |
| 199701102104 | 199603202139 | 199702071703 |
| 199701121715 | 199603221750 | 199702071845 |
| 199701121857 | 199603221932 | 199702072027 |
| 199701122039 | 199603222114 | 199702072209 |
| 199701122221 | 199701051841 | 199702091821 |
| 199702041740 | 199701052023 | 199702092003 |
| 199702041922 | 199701052205 | 199702092145 |
| 199702042104 | 199701071816 | 199701071958 |
| 199702061716 | 199701072140 | 199701091752 |

$$\begin{aligned}
 f_1 &= c^{-1} \sec \psi \left[1 - \exp(-cs \cos \psi) + \frac{16f_3 \tan^2 \psi}{9\pi 2cR_T} \right], \\
 f_2 &= a^{-1} \sec \psi \left[1 - \exp(-as \cos \psi) + \frac{16f_4 \tan^2 \psi}{9\pi 2aR_T} \right], \\
 f_3 &= (c^2 s^2 \cos^2 \psi + 2cs \cos \psi + 2) \exp(-cs \cos \psi) - 2, \\
 f_4 &= (a^2 s^2 \cos^2 \psi + 2as \cos \psi + 2) \exp(-as \cos \psi) - 2.
 \end{aligned} \tag{A3}$$

For $\psi = 90^\circ$ the reader is referred to the cited paper.

APPENDIX B: DMSP ORBITS USED

Table B1 gives the orbits of the DMSP satellite *F12* used in the composite radiance calibrated image.

This paper has been typeset from a \TeX/L\AA\TeX file prepared by the author.